Sensitivity of magnetohydrodynamic simulations of Joule-heated conductors to the vaporization curve in equations of state

Seth E. Kreher,[1,2,*] Christopher L. Rousculp,[1] Bruno S. Bauer,[2] Trevor M. Hutchinson,[3] Aidan W. Klemmer,[2] Charles E. Starrett,[1] and Edmund P. Yu[4]

[1]*Los Alamos National Laboratory, Los Alamos, New Mexico 87545, USA*

[2]*Department of Physics, University of Nevada, Reno, Nevada 89506, USA*

[3]*Lawrence Livermore National Laboratory, Livermore, California, 94551-0808, USA*

[4]*Sandia National Laboratory, P. O. Box 5800, Albuquerque, New Mexico 87185-1186, USA*

(Received 2 March 2023; accepted 3 May 2024; published 4 June 2024)

Magnetohydrodynamic (MHD) simulations of electrically exploded aluminum and copper rods demonstrate a technique to validate equations of state (EOS) for rapidly Joule-heated conductors. The balance of internal and magnetic forces at the conductor-insulator interface drives the metal there along the vaporization phase boundary. Variations between critical points and vaporization curves in existing models predict differing densities and temperatures in MHD simulations for these models. The inclusion of Maxwell constructs in the liquid-vapor biphase region of the EOS caused the rod surface to vaporize earlier in time than unmodified tables with van der Waals loops. Velocimetry of recent experiments is used to validate the location of the vaporization curve in existing EOS models and differentiate between the vapor dome treatments. Dielectric coatings applied to the metal surface restricted the conductor's expansion and diverted the metal into the warm dense matter regime.

DOI: 10.1103/PhysRevE.109.065202

I. INTRODUCTION

This article demonstrates a technique to validate equations of state (EOS) when modeling conductors under intense Joule heating by fast current pulses. Pulsed power is a proven method to create strong Lorentz forces that drive implosions in Z-pinch liners for fusion [1–3] and accelerate flyer plates for dynamic material science experiments [4–6]. Exploding thin metal wires and foils via Joule heating are used in electrical initiators of high explosives [7,8] and for opening and closing switches in high-current circuits [9]. The dynamic conductors are, however, susceptible to hydrodynamic and magnetohydrodynamic (MHD) instabilities that distort the metal and degrade the performance of these platforms [10,11].

Numerical simulations using the single-fluid MHD system of equations can capture the dynamics of these systems but require accurate EOS and electrical conductivity (ECON) models. Tabular equation of state models used in these calculations can vary widely in the expanded metal regime, i.e., along the vaporization phase boundary and near the critical point. Because this region is where the unstable metal surfaces traverse, the different pressure, density, and temperature relationships between EOS models can cause large variations in the predicted instability growth rates [11]. As a result, simulations are often limited by these models, which makes designing future pulsed power experiments incredibly difficult when the models have not been properly validated for this region of phase space.

Here simulated electrically exploded aluminum and copper rods show the conductor at the conductor-vacuum interface tracks the vaporization phase boundary of the EOS used. Moreover, the velocity of this metal surface (in the fluid approximation, i.e., mean radial location of the outermost ~100 atomic layers) over time depends very strongly on the trajectory it takes through density-temperature phase space. Experimental velocimetry measurements of these rods could then be used to validate the location of the vaporization curve in EOS models—providing for more accurate MHD simulations of pulsed current applications.

II. THEORY

The single-fluid resistive MHD model [Eqs. (1)–(4)] captures the relevant physics for conductors driven by intense currents [12,13]. The single-fluid model approximates the ion and electron species as being in equilibrium which is valid when the electron-ion collision frequency, ν_{ei}, is much larger than the ion gyrofrequency, ω_{ci}. For the Mykonos rod simulations presented here, $\omega_{ci}/\nu_{ei} \leqslant 10^{-2} \ll 1$. The MHD equations,

$$\frac{D\rho}{Dt} = -\rho(\nabla \cdot \boldsymbol{u}), \tag{1}$$

$$\rho\frac{D\boldsymbol{u}}{Dt} = -\nabla p + \nabla \cdot \underline{\underline{s}} + \boldsymbol{j} \times \boldsymbol{B}, \tag{2}$$

$$\frac{D(\rho\epsilon)}{Dt} = -p(\nabla \cdot \boldsymbol{u}) + \eta j^2, \tag{3}$$

$$\frac{\partial \boldsymbol{B}}{\partial t} = -\nabla \times \eta\boldsymbol{j} + \nabla \times (\boldsymbol{u} \times \boldsymbol{B}), \tag{4}$$

include material strength and solve for the mass density ρ, fluid velocity $\boldsymbol{u}$, and specific internal energy ϵ [13–15] while the magnetic field $\boldsymbol{B}$ evolves according to Maxwell's equations. $D/Dt(\ldots)$ represents the material or convective

*kreher@lanl.gov

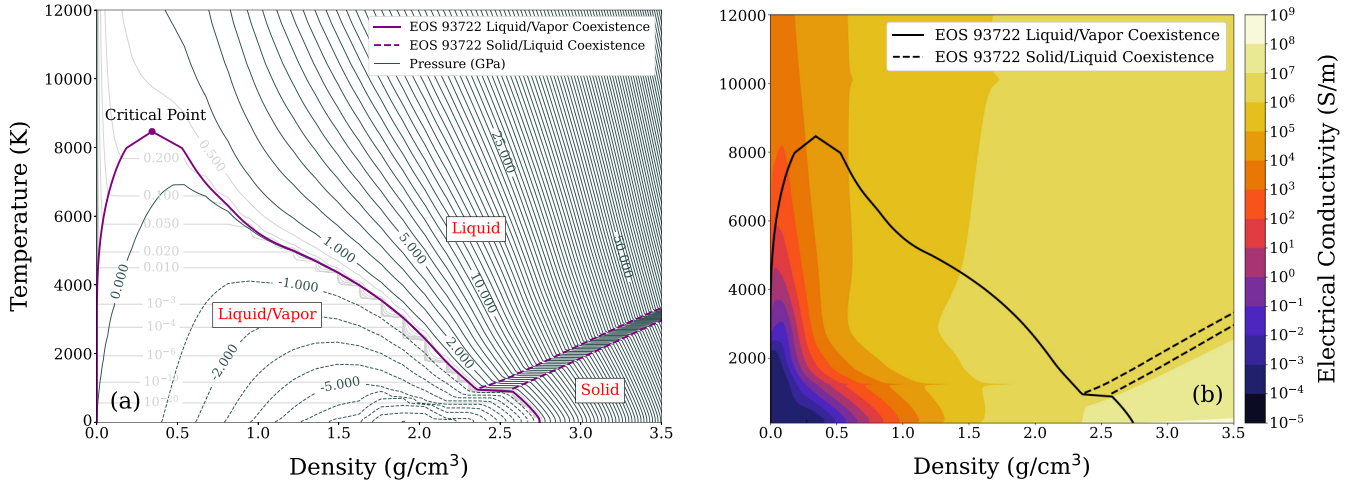

FIG. 1. (a) The structure from a recent EOS for Al [18] in the region of interest for this study. The region between the vapor and liquid phases is broad and is commonly referred to as the vapor dome. At its apex resides the critical point (CP), above which the liquid and vapor states are nearly indistinguishable. To the left of the critical point the vapor dome is bounded by the condensation curve, and to the right the vaporization curve. Under the vapor dome, so-called van der Waals loops exist including negative pressures (dark gray, dashed). Maxwell constructs (light gray) are often implemented where isobars are also isotherms. The melt and solidification lines are seen to the lower right. (b) The corresponding ECON model for Al where the solid phase boundaries align with those in (a).

derivative in the Lagrangian frame of reference [16], pp. 28-29. The electromagnetic equations are reduced by ignoring displacement currents such that the current density $\boldsymbol{j} = \nabla \times \boldsymbol{B}/\mu$, where μ is the permeability of the conductor and by including the resistive Ohm's law ($\eta \boldsymbol{j} = \boldsymbol{E} + \boldsymbol{u} \times \boldsymbol{B}$) [16], p. 32. For good conductors like aluminum, μ can be approximated by the permeability of free space, $\mu_0 = 4\pi \times 10^{-7}$ H/m.

The stress deviator tensor, $\underline{\underline{s}}$, includes the off-diagonal terms of the mechanical stress tensor and accounts for material strength. Once the material melts, these terms disappear and $\nabla \cdot \underline{\underline{s}}$ goes to zero. Strength was included in all the numerical calculations presented in this paper using the Preston-Tonks-Wallace flow stress model [17]. When the strength model was removed, though, it only varied the expansion rate of the exploding rod by ∼5 m/s before the surface melted.

The system is closed with an EOS model providing the pressure, $p(\rho, T)$ [Fig. 1(a)] and temperature, $T(\rho, \epsilon)$, as well as an isotropic ECON model, $\sigma(\rho, T)$ [Fig. 1(b)]. The conductivity σ of the metal is the inverse of its resistivity η. Thermal conduction was neglected here as the radial melt wave outpaces the relatively slow diffusion of heat. Finally, radiative cooling was also ignored for the low-temperature regime discussed in this paper. Even for 10 eV temperatures, the blackbody radiative heat flux density ($\sigma_{\mathrm{SB}} T^4$) of the rod surface was 10^8 times smaller than the Joule heating rate.

Variability between EOS models near the critical point has a significant impact for the expansion dynamics [19] and instability development [11] of Joule-heated conductors and is an important area of development. For computation, the models are commonly represented in data tables in SESAME format [20]. To cover the wide range of phase space needed for the numerical simulations, the EOSs necessarily combine multiple analytic and calculated models with varying domains of applicability. For example, solid and liquid states are usually constructed from density functional theory (DFT) calculations and constrained by experimental measurements as in Ref. [19]. At lower densities relevant to the expanded metal regime, however, a Lennard-Jones model has been implemented to connect to the DFT data [21]. The Lennard-Jones analytic model is fit to the high-density material data which introduces discrepancies in the predicted critical points and vaporization and condensation phase boundaries between equations of state. This is demonstrated in the set of three Al EOSs used in this article. The standard deviations of the set's critical point density (0.0973 g/cm^3) and temperature (1107 K) were roughly 25% of the average density and 15% of the average temperature. The critical point and vaporization phase boundary locations are indicative of the different pressure landscapes of the models in the expanded metal regime [Fig. 1(a)]. For an electrically exploded metal, each EOS model would predict different densities and temperatures of the conductor as it expanded. This pressure-density relationship defined by the EOS impacts the growth rates of fluid instabilities by exacerbating density perturbations they are unstable to over time.

The Lennard-Jones model also introduces a thermodynamically unstable region where $\partial p/\partial \rho < 0$ in the central region of the liquid-vapor biphase. This unstable region models spinodal decomposition of the mixed phase into regions of pure vapor and liquid. To either side of this unstable region, the model represents the metastable superheated liquid and supercooled vapor states. Material held in these metastates will eventually decompose via nucleation of vapor bubbles or liquid droplets in the material [22]. Once the metastate has decomposed, the stable liquid-vapor mixed state is accurately represented by Maxwell constructs [23]. As a result, two versions of an EOS often exist: the unmodified vapor dome model that is referred to as a van der Waals (VdW) model and the Maxwell constructed (MC) vapor dome [Fig. 1(a)]. The validity of either model depends heavily on the timescale of the problem as compared to the nucleation timescale for the metastable states.

III. MHD SIMULATIONS

Large-diameter cylindrical metal rods with an initial radius ($R \approx 400$ μm) much larger than the electrical skin depth ($\delta \approx 46$ μm) were fielded at the Mykonos [24] linear transformer driver ($t_{\rm rise} \sim 80$ ns, $I_{\rm pk} \sim 850$ kA). High-precision velocimetry with a ∼52-μm spot size (much smaller than the rod diameter) was fielded to characterize the rods' surface expansion [25–27] and has proven to be a valuable data set to compare to numerical simulations. In order to understand the complex evolution of the high-current rod system in terms of the experimental data, single-fluid MHD simulations using the multimaterial, Lagrangian FLAG code [28,29] were conducted. One-dimensional simulations of the rod's radius where a single axial computational cell was included were performed to calculate the bulk evolution of the rod without surface instabilities. The experimentally measured current traces were applied as the magnetic field boundary condition for all metal rods. An initial mesh resolution of 10 nm on the rod surface was necessary for a converged solution for the ∼100X expansion from solid ($\rho_0 = 2.7$ g/cm^3) to vapor ($\rho \sim 10^{-2}$ g/cm^3) densities.

Three tabular aluminum equation of state models were tested when simulating the Mykonos rods—each with a VdW and MC version. They were chosen to span the development of EOS tables and identify the features in an EOS model that impact calculations of exploded metal. SESAME 3718 is a historical table used for imploding liners that exhibited instability growth better than previous tables [11]. However, it does not include a solid-liquid biphase region in contrast with the other two tables. SESAME 3720 is the current workhorse for pulsed power calculations. It was developed primarily for high-pressure condensed states but offered some improvements for the expanded regime as shown by the critical point location rising in temperature significantly [30]. Finally, EOS 93722 is the latest table developed of the three and represents the current state-of-the-art model. It also focused heavily on the high-pressure states—including the multiple solid allotropes for aluminum in addition to a liquid state and an improved treatment of the warm dense matter regime [18]. It also included exploded aluminum foil experimental data in the expanded metal region of phase space. This all led to the most accurate critical point location and expanded aluminum treatment of the models here and a significant change in the vaporization phase boundary compared to 3720.

In the Lagrangian MHD calculations, the balance of the internal ($-\nabla p$) and magnetic ($\boldsymbol{j} \times \boldsymbol{B}$) forces at the conducting-nonconducting boundary drives the metal at this interface along a quasi-isobaric expansion that coincides with the vaporization curve of the EOS. While the pressure evolution of the outer aluminum zones was largely consistent for every EOS model tested, the densities and temperatures corresponding to this pressure evolution varied widely between them [Fig. 2(a)]. Because the expansion velocity at the rod's surface is proportional to the expanding surface layer's change in density, experimental velocimetry can distinguish between the density evolution prescribed by each EOS model. Moreover, the pressure in the metal approaches zero (i.e., the surrounding vacuum pressure) for radii approaching the surface of the uncoated rods. The density and temperature evolution at the surface are then correlated and velocimetry measurements can be used validate EOS models (density and temperature) for expanding metal rods near the zero-pressure isobar. Figure 2(b) shows the divergent surface velocities of simulations using each tabular equation of state. For the aluminum Mykonos rods, the VdW version of EOS 93722 predicted the closest expansion rate to the experimental PDV data.

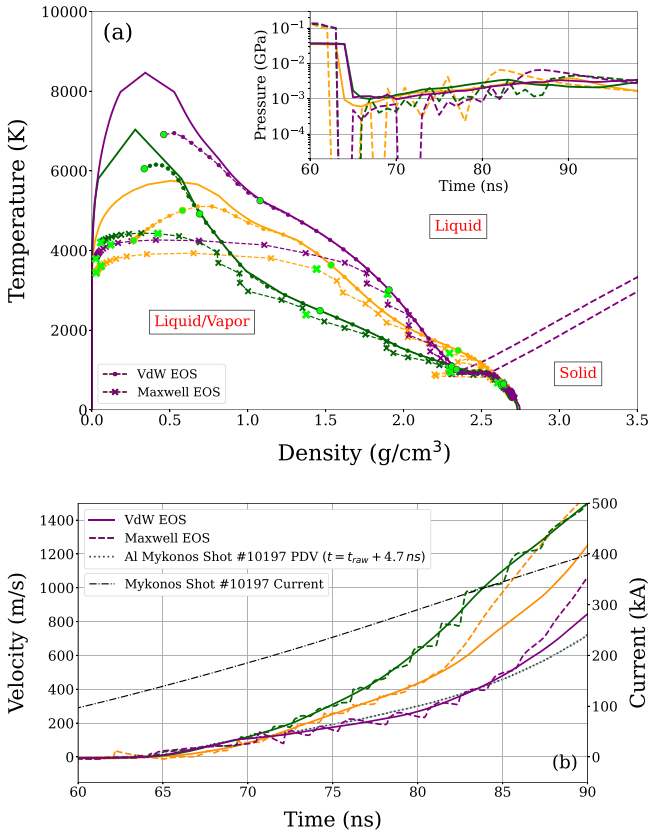

FIG. 2. (a) MHD Al rod surface trajectories in density, temperature space are plotted every ns from $t = 0$ to 100 ns over the phase boundaries of the models used: EOS 93722 [purple, CP = (0.343 g/cm^3, 8463 K)] [18], SESAME 3720 [green, CP = (0.278 g/cm^3, 7036 K)] [30], and SESAME 3718 [orange, CP = (0.510 g/cm^3, 5751 K)]. Every 10 ns is marked using lime green starting from 60 ns in the bottom right to 100 ns. Inset: The pressure of the outermost cell is plotted over time for VdW (solid) and Maxwell (dashed) EOS models. (b) The simulated surface velocities are compared against experimental PDV measurements: SESAME 3720 (green, top curves), SESAME 3718 (orange, middle curves), and EOS 93722 (purple, bottom curves near PDV). A systematic timing offset between the PDV and B-dot diagnostics was corrected for by shifting the PDV data +4.7 ns.

Using Maxwell constructs in the EOS had a significant affect on the rod's (ρ, T) trajectory—causing the metal surface to vaporize earlier than the VdW counterpart. Maxwell constructs eliminate the thermodynamically unstable region where $\partial p/\partial \rho < 0$ by setting a constant pressure for a given temperature under the vapor dome. For the liquid-vapor region adjacent to the liquid phase, the Maxwell construct pressure is by definition greater than the VdW model's pressure due

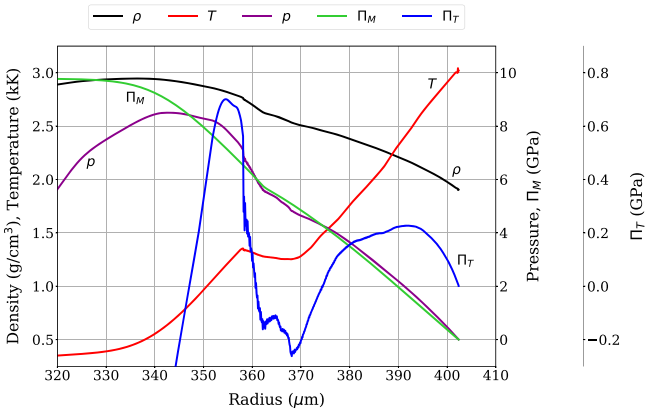

FIG. 3. Radial profiles of the mass density, ρ, temperature, T, material pressure, p, magnetic energy density, Π_M, and total force density potential, Π_T, for an uncoated Al Mykonos rod using the VdW EOS 93722 at $t = 80$ ns.

to this process. Because the metal surface's trajectory is set by the pressure value of the EOS, calculations using the Maxwell constructed models will divert under the vapor dome at lower temperatures and earlier in time than when using the VdW EOS [Fig. 2(a)]. Furthermore, as the surface velocity follows the change in density of the outer zone, the earlier vaporization appears as a rapid acceleration of the Al surface that diverges from the VdW prediction.

The magnetic force density potential in cylindrical geometry, Π_M, is the magnetic equivalent to the hydrodynamic pressure, p, and was used to determine the relative strengths of internal and magnetic forces in the expanding surface layer of the rod. In Cartesian geometry, Π_M is equivalent to the magnetic pressure, $p_M = B^2/2\mu_0$. It was calculated at a location in the rod by spatially integrating Eq. (2) from the outer conducting boundary at $r = R$ to the radius r of interest. For a 1D right-circular cylinder like the Mykonos rod calculations, this results in Eq. (5),

$$\int_r^R \rho \frac{Du_{r'}}{Dt} dr' = p(r) - \int_r^R j_z B_\phi dr' - p(R). \tag{5}$$

Here $p(R)$ is the pressure of the material outside the rod at the conductor-insulator boundary. For a rod surrounded in vacuum, $p(R) \approx 0$, but for a conducting rod coated with a dielectric, the pressure of the coating at the boundary evolves over time according to the expanding metal beneath it: $p(R) = p(R, t)$.

Π_T represents the total force density potential and is defined as the difference between the internal force density potential (i.e., material pressure p) and magnetic radial force density potential, $\Pi_M \equiv \int_r^R j_z B_\phi dr'$. Substituting $\Pi_T \equiv p - \Pi_M$ into the momentum equation yields Eq. (6) where $-\nabla \Pi_T$ determines the local forces in the rod,

$$\rho \frac{D\boldsymbol{u}}{Dt} = -\nabla \Pi_T. \tag{6}$$

Figure 3 shows the competition of the magnetic and material contributions to $\Pi_T(r)$ in a MHD simulation of an Al Mykonos rod at 80 ns. In the outer 10 μm, $d\Pi_T/dr < 0$ and the rod is exploding. From 354 μm in, the total potential gradient is positive and this section of the rod is being compressed. Between these regimes, the radial melt wave is traversing the rod's radius. Inside the solid-liquid biphase, the Joule heating is diverted to paying off the latent heat of fusion and the pressure of the material here could not keep up with the rising magnetic force density potential. This generated a local minimum in Π_T where the solid metal underneath and liquid metal outside both acted to compress the melt transition region. The melt wave trailed the diffusion of current in the rod, though, and the fast transit of the melting region through the rod reduced the compression of material undergoing the solid-to-liquid phase transition.

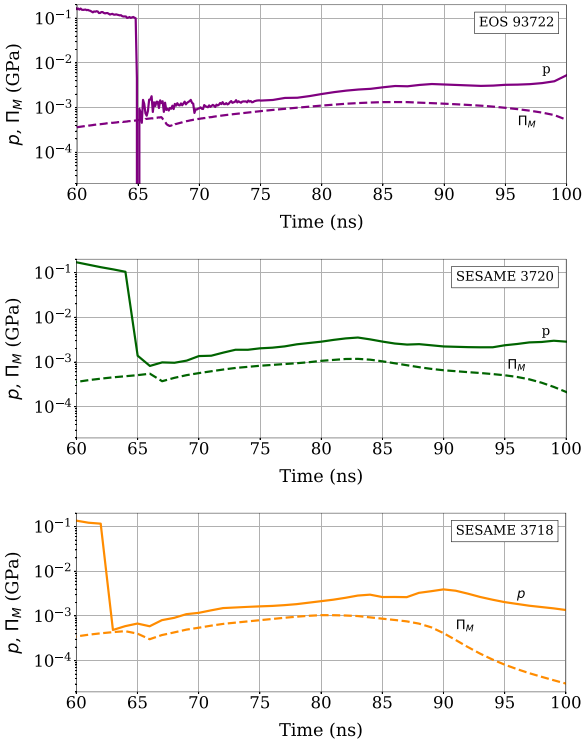

FIG. 4. Material pressure (solid) and magnetic force density potential, Π_M, (dashed) are plotted for the outer MHD computational zone over time using various aluminum VdW equations of state: (top) EOS 93722, (middle) SESAME 3720, and (bottom) SESAME 3718.

While the magnetic force was too small to overcome the rod's expansion, it was an effective brake on the aluminum surface. In Fig. 4, the pressure and magnetic force density potential of the outermost aluminum zone are shown through the expansion of the rod along the vaporization curve. As in Fig. 3, Π_M was similar in magnitude to p and prevented rapid expansion. Because the pressure and magnetic force density potential in the surrounding vacuum are identically zero, the difference of p and Π_M in Fig. 4 is proportional to the gradient of the total force density potential across the conductor-insulator boundary and therefore the acceleration of the rod surface. After melting, the material strength is removed and the pressure drops considerably before evolving along a similar contour as $\Pi_M(t)$ in the outer zone. This was due to the internal pressure being more sensitive to changes in density than Π_M. The Joule heating in the expanding rod

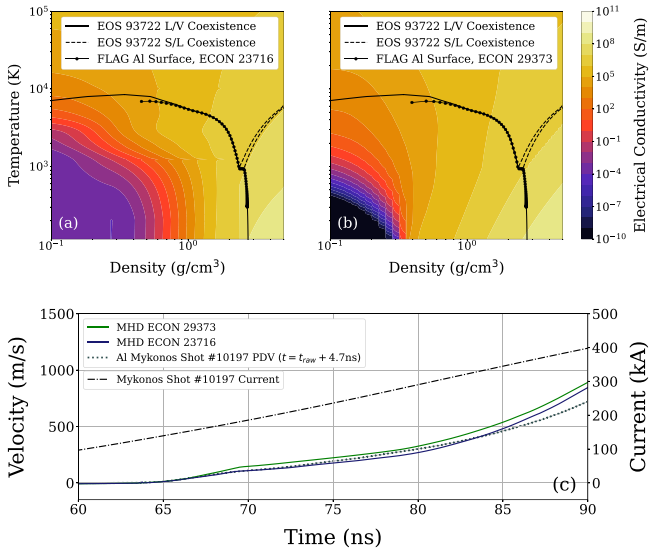

FIG. 5. MHD Al rod surface trajectories using EOS 93722 and two modern Al ECON tables: (a) 23716 and (b) 29373. (c) Simulated expansion velocities for both calculations are compared against experimental PDV measurements.

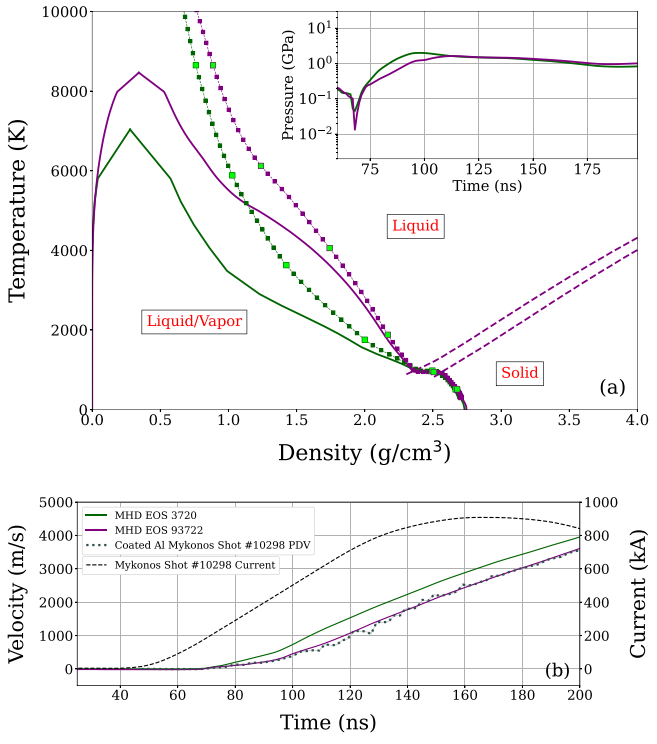

FIG. 6. (a) The outer zone trajectories of a simulated Al rod coated with 35 μm of Parylene-N are overlaid on the phase boundaries for EOS 93722 [purple, CP = (0.343 g/cm^3, 8463 K)] and SESAME 3720 [green, CP = (0.278 g/cm^3, 7036 K)]. Every 10 ns is marked in lime green starting from 60 ns in the bottom right to 110 ns toward the top of the simulation trajectory. Inset: The pressure of these trajectories is plotted over time. (b) The simulated surface velocities are compared to the analyzed experimental PDV data.

raised the aluminum temperature and thus pressure much faster than Π_M. As the material expanded from the resulting internal forces, though, the pressure dropped faster with density than the magnetic potential until it reached a value that maintained a relatively constant relationship between the two potentials. This resulted in a balancing of the internal and magnetic forces in the Mykonos rods to an approximately constant acceleration during the 20–30 ns the surface followed the vaporization curve after melting.

The MHD simulations were not as sensitive to variations in electrical conductivity as they were to the location of the EOS vaporization curve. In Fig. 5, calculations using two modern ECON tables in conjunction with EOS 93722 were compared. ECON 23716 was specifically developed to also match the melt phase boundary in EOS 93722 while ECON 29373 was developed independently from the equation of state. The resulting discrepancies between the tables' conductivities near the solid-liquid biphase altered the Joule heating rate on the Al surface while it was melting. ECON 29373 predicted a larger heating rate that decreased the time spent in the biphase and therefore increased the rate at which the zone expanded. This accelerated the rod's surface to larger velocities during the melting process than when using ECON 23716 with a lower Joule heating rate [Fig. 5(c)]. The conductivity models did not, however, impact the phase space trajectory of the rod nor did they vary the acceleration of the rod surface as it traversed along the vaporization phase boundary.

Coating the rod with a layer of the dielectric Parylene-N inertially tamped the metal's expansion and caused the surface to divert from the vaporization curve to a high-pressure liquid and later into the warm dense matter regime [33]. As the rod expanded, it compressed the plastic which then raised the boundary condition pressure $p(R)$ and caused the metal

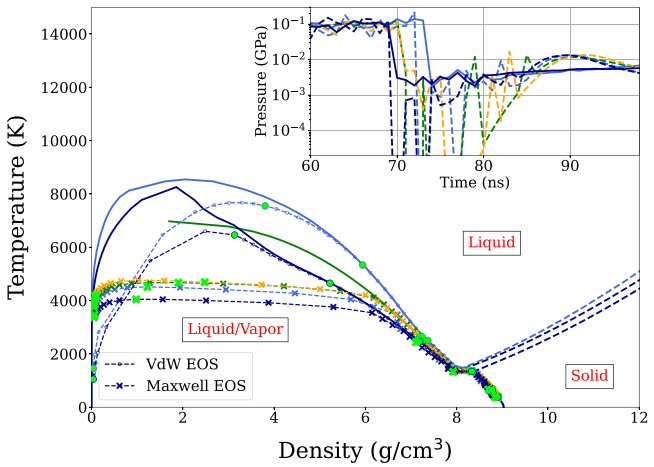

FIG. 7. MHD simulated uncoated Cu surface trajectories in density, temperature space are plotted every ns for the EOS models used: SESAME 3337 [light blue, CP = (2.04 g/cm^3, 8544 K)] [31], EOS 93338 [dark blue, CP = (1.85 g/cm^3, 8255 K)], and EOS 3325 [green, CP = (1.70 g/cm^3, 6972 K)] [32]. EOS 3325 was also tested with ECON 23335 [orange (light gray) crosses]. Every 10 ns is marked using lime green from 60 ns in the bottom right to 100 ns. Inset: The pressure of the outermost zone for each calculation is plotted over time for VdW (solid) and Maxwell (dashed) EOS models.

to overshoot the critical point. This allowed the metal in the coated simulations to avoid the uncertainties in the EOS models associated with the critical point location and resulted in a more accurate surface acceleration from 90 ns on. However, the Al models still vary enough near the melting transition to impact the early surface acceleration such that they predict different velocities later in time. The steeper $dT/d\rho$ trajectory in EOS 93722 slowed the velocity earlier in the rod's expansion and resulted in a closer fit to the PDV data once again (Fig. 6).

Finally, simulations of similar exploding Cu rods exhibited the same strong sensitivity to the equation of state vaporization curve. Figure 7 shows the phase space trajectories for the outer computational zones of pure Cu Mykonos rod calculations using various EOS and ECON tables. Just like the aluminum rods, the outer Lagrangian zone of the conductor followed a specific pressure vs time evolution. The calculations using equations of state with Maxwell constructs also diverted under the vapor dome earlier in time and at lower temperatures than their VdW counterparts. These varying trajectories again correspond to different predicted surface velocities with $v_{3337} < v_{3325} < v_{93338}$ before the surface vaporized; however, no experimental PDV data for this uncoated Cu rod was available to the authors to validate any particular EOS for the expanded metal regime.

IV. CONCLUSIONS

The use of experimental velocimetry to validate MHD simulations of Joule-heated conductors demonstrates a simple, effective method to improve the tabular EOS models currently in use for the expanded metal regime. This technique identified what general shape the vaporization curve for aluminum should exhibit with EOS 93722 providing a close fit relative to the other models tested. Because the force balance at the metal surface dictated the pressure of the outermost computational cell, increasing the pressures under the vapor dome in a Maxwell constructed EOS lead to an earlier vaporization of the conductor's surface. While the inclusion of a plastic tamper diverted the density and temperature of the metal surface away from the vaporization curve to warm dense matter, the sensitivity of the calculation to the EOS model used was consistent. The continued detailed comparison between MHD calculations and high-fidelity PDV data of exploding conductors is therefore a rich area for research into the properties and evolution of metals driven by intense current pulses.

ACKNOWLEDGMENTS

The authors sincerely thank Will Neal, Nathaniel Shaffer, Irvin Lindemuth, Kyle Cochrane, and Jeff Peterson for the many useful discussions aiding this work. This work was supported by the U.S. Department of Energy through NNSA Awards DE-NA0003870 and DE-NA0004136 and through Los Alamos National Laboratory is operated by Triad National Security, LLC, for the National Nuclear Security Administration of U.S. Department of Energy (Contract No. 89233218CNA000001). Part of this work was performed under the auspices of the U.S. Department of Energy by Lawrence Livermore National Laboratory under Contract No. DE-AC52-07NA27344.

[1] M. M. Basko, A. J. Kemp, and J. Meyer-ter Vehn, Nucl. Fusion **40**, 59 (2000).
[2] S. A. Slutz, M. C. Herrmann, R. A. Vesey, A. B. Sefkow, D. B. Sinars, D. C. Rovang, K. J. Peterson, and M. E. Cuneo, Phys. Plasmas **17**, 056303 (2010).
[3] M. R. Gomez, S. A. Slutz, A. B. Sefkow, D. B. Sinars, K. D. Hahn, S. B. Hansen, E. C. Harding, P. F. Knapp, P. F. Schmit, C. A. Jennings, T. J. Awe, M. Geissel, D. C. Rovang, G. A. Chandler, G. W. Cooper, M. E. Cuneo, A. J. Harvey-Thompson, M. C. Herrmann, O. Johns, D. C. Lamppa *et al.*, Phys. Rev. Lett. **113**, 155003 (2014).
[4] J. R. Asay, AIP Conf. Proc. **505**, 261 (2000).
[5] J.-P. Davis, C. Deeney, M. D. Knudson, R. W. Lemke, T. D. Pointon, and D. E. Bliss, Phys. Plasmas **12**, 056310 (2005).
[6] J.-P. Davis, J. Appl. Phys. **99**, 103512 (2006).
[7] P. J. Rae and P. M. Dickson, Proc. R. Soc. A. **475**, 20190120 (2019).
[8] W. Neal and C. Garasi, AIP Conf. Proc. **1793**, 080008 (2017).
[9] I. R. Lindemuth, R. S. Caird, J. H. Goforth, H. Oona, and R. E. Reinovsky, J. Appl. Phys. **67**, 7111 (1990).
[10] D. B. Sinars, S. A. Slutz, M. C. Herrmann, R. D. McBride, M. E. Cuneo, K. J. Peterson, R. A. Vesey, C. Nakhleh, B. E. Blue, K. Killebrew, D. Schroen, K. Tomlinson, A. D. Edens, M. R. Lopez, I. C. Smith, J. Shores, V. Bigman, G. R. Bennett, B. W. Atherton, M. Savage *et al.*, Phys. Rev. Lett. **105**, 185001 (2010).
[11] W. L. Atchison, P. J. Turchi, and D. S. Lemons, in *Proceedings of the 2006 IEEE International Conference on Megagauss Magnetic Field Generation and Related Topics, Santa Fe, NM* (IEEE, Piscataway, NJ, 2006), pp. 57–67.
[12] A. Jeffrey, *Magnetohydrodynamics* (John Wiley & Sons, New York, 1966).
[13] V. I. Oreshkin, Phys. Plasmas **15**, 092103 (2008).
[14] J. D. Pecover and J. P. Chittenden, Phys. Plasmas **22**, 102701 (2015).
[15] V. I. Oreshkin, S. A. Chaikovsky, I. M. Datsko, N. A. Labetskaya, G. A. Mesyats, E. V. Oreshkin, N. A. Ratakhin, and D. V. Rybka, Phys. Plasmas **23**, 122107 (2016).
[16] H. E. Knoepfel, *Magnetic Fields: A Comprehensive Theoretical Treatise for Practical Use* (John Wiley & Sons, New York, 2000).
[17] D. L. Preston, D. L. Tonks, and D. C. Wallace, J. Appl. Phys. **93**, 211 (2003).
[18] T. Sjostrom, S. Crockett, and S. P. Rudin, Phys. Rev. B **94**, 144101 (2016).
[19] J. Clerouin, P. Noiret, V. N. Korobenko, and A. D. Rakhel, Phys. Rev. B **78**, 224203 (2008).
[20] S. P. Lyon and J. D. Johnson, *SESAME: The Los Alamos National Laboratory Equation of State Database*, Tech. Rep. LA-UR-92-3407 (Los Alamos National Laboratory, Los Alamos, NM, 1992).

[21] D. A. Rehn, C. W. Greeff, D. G. Sheppard, and S. Crockett, *Using Density Functional Theory to Construct Multiphase Equations of State: Tin as an Example*, Tech. Rep. LA-UR-20-29170 (Los Alamos National Laboratory, Los Alamos, NM, 2020).

[22] D. S. Corti and P. G. Debenedetti, Chem. Eng. Sci. **49**, 2717 (1994).

[23] J. C. Maxwell, Nature (London) **11**, 357 (1875).

[24] M. G. Mazariakis, W. E. Fowler, K. L. LeChien, F. W. Long, M. K. Matzen, D. H. McDaniel, R. G. McKee, C. L. Olson, J. L. Proter, S. T. Rogowski, K. W. Struve, W. A. Stygar, J. R. Woodworth, A. A. Kim, V. A. Sinebryukhov, R. M. Gilgenbach, M. R. Gomez, D. M. French, Y. Y. Lau, J. Zier *et al.*, IEEE Trans. Plasma Sci. **38**, 704 (2010).

[25] T. M. Hutchinson, T. J. Awe, B. S. Bauer, K. C. Yates, E. P. Yu, W. G. Yelton, and S. Fuelling, Phys. Rev. E **97**, 053208 (2018).

[26] T. M. Hutchinson, T. J. Awe, B. S. Bauer, D. H. Dolan, J. R. Pillars, B. T. Hutsel, E. P. Yu, A. W. Klemmer, and S. E. Kreher, Phys. Plasmas **27**, 052705 (2020).

[27] T. M. Hutchinson, T. J. Awe, B. S. Bauer, B. T. Hutsel, D. A. Yager-Elorriaga, K. C. Yates, A. W. Klemmer, M. W. Hatch, S. E. Kreher, E. P. Yu, and M. Gilmore, J. Appl. Phys. **130**, 153302 (2021).

[28] D. E. Burton, *Consistent Finite-volume Discretization of Hydrodynamic Conservation Laws for Unstructured Grids*, Tech. Rep. UCRL-JC-118788 (Lawrence Livermore National Laboratory, Livermore, CA, 1994).

[29] K. Lipnikov, J. Reynolds, and E. Nelson, J. Comput. Phys. **247**, 1 (2013).

[30] S. D. Crockett, *Analysis of SESAME 3720, a New Aluminum Equation of State*, Tech. Rep. LA-UR-04-6442 (Los Alamos National Laboratory, Los Alamos, NM, 2004).

[31] J. H. Peterson, K. G. Honnell, C. Greeff, J. D. Johnson, J. Boettger, and S. Crockett, AIP Conf. Proc. **1426**, 763 (2012).

[32] K. R. Cochrane, R. W. Lemke, Z. Riford, and J. H. Carpenter, J. Appl. Phys. **119**, 105902 (2016).

[33] F. Graziani, M. P. Desjarlais, R. Redmer, and S. B. Trickey, *Frontiers and Challenges in Warm Dense Matter* (Springer, Berlin, 2014).